Published for SISSA by Springer

Received: *August 29, 2018*
Accepted: *October 5, 2018*
Published: *October 24, 2018*

JHEP10(2018)150

Measurement of the form factors of charged kaon semileptonic decays

The NA48/2 collaboration

E-mail: Dmitri.Madigojine@cern.ch, Sergey.Shkarovskiy@cern.ch

Abstract: A measurement of the form factors of charged kaon semileptonic decays is presented, based on 4.4×10^6 $K^\pm \to \pi^0 e^\pm \nu_e$ ($K^\pm_{e3}$) and 2.3×10^6 $K^\pm \to \pi^0 \mu^\pm \nu_\mu$ ($K^\pm_{\mu 3}$) decays collected in 2004 by the NA48/2 experiment. The results are obtained with improved precision as compared to earlier measurements. The combination of measurements in the $K^\pm_{e3}$ and $K^\pm_{\mu 3}$ modes is also presented.

Keywords: Fixed target experiments, Rare decay

ArXiv ePrint: 1808.09041

https://doi.org/10.1007/JHEP10(2018)150

Contents

JHEP10(2018)150

1 Introduction

The NA48/2 experiment at the CERN SPS was designed primarily to search for direct CP violation in $K^{\pm}$ decays to three pions [1]. It used simultaneous K^+ and K^- beams with momenta of 60 GeV/c. Data were collected in 2003–2004, providing 2×10^9 reconstructed $K^{\pm} \to 3\pi$ decays. Additionally, a data set was recorded at reduced beam intensity using a minimum bias trigger during a 52-hour long data-taking period in 2004.

The $K^{\pm} \to \pi^0 l^{\pm} \nu$ ($K^{\pm}_{l3}$, with $l = e, \mu$) decays contribute to the precise determination of the CKM matrix element $|V_{\rm us}|$ [2], which requires the knowledge of both branching ratios and form factors (FFs). Measurements of the $K^{\pm}_{l3}$ vector f_+ and scalar f_0 FFs based on the above minimum bias data set are presented here.

In absence of electromagnetic effects, the differential $K^{\pm}_{l3}$ decay rate is described in the (E^*_l, E^*_π) Dalitz plot as [3]:

$$\frac{d^2\,\Gamma(K^{\pm}_{l3})}{dE^*_l\,dE^*_\pi} \;=\; \rho(E^*_l, E^*_\pi) \;=\; N\left(A_1\,|f_+(t)|^2 + A_2\,f_+(t)f_-(t) + A_3\,|f_-(t)|^2\right), \qquad (1.1)$$

where E_l^* and E_π^* are the lepton and pion energies in the kaon rest frame; t is the 4-momentum transfer to the leptonic system; N is a numerical factor; $f_-(t) = (f_0(t) - f_+(t))(m_K^2 - m_{\pi^0}^2)/t$; m_K and m_{π^0} are the charged kaon and neutral pion masses [4]. The kinematic factors are

$$\begin{aligned} A_1 &= m_K\ (2\,E_l^*\,E_\nu^* - m_K(E_\pi^{*,\max} - E_\pi^*)) + m_l^2\ ((E_\pi^{*,\max} - E_\pi^*)/4 - E_\nu^*)\,, \\ A_2 &= m_l^2\ (E_\nu^* - (E_\pi^{*,\max} - E_\pi^*)/2)\,, \\ A_3 &= m_l^2\,(E_\pi^{*,\max} - E_\pi^*)/4. \end{aligned} \tag{1.2}$$

Here $E_\pi^{*,\max} = (m_K^2 + m_{\pi^0}^2 - m_l^2)/2\,m_K$, m_l is the charged lepton mass, and $E_\nu^* = m_K - E_l^* - E_\pi^*$ is the neutrino energy in the kaon rest frame. For $K_{e3}^\pm$ decays, the factors A_2 and A_3, which are proportional to m_l^2, become negligible and only the vector FF contributes within the experimental precision.

The FF parameterizations considered are described in table 1. They include a Taylor expansion in the variable $t/m_{\pi^+}^2$ [4], where m_{π^+} is the charged pion mass, a parameterization assuming vector and scalar pole masses M_V and M_S [5, 6] and a more physical dispersive parameterization [7]. The Taylor expansion is affected by large correlations between the measured parameters. The pole parameterization has a physical interpretation for $f_+(t)$ related to the $K^*(892)$ scattering pole, but not for $f_0(t)$ with no corresponding pole. The dispersive parameterization makes use of general chiral symmetry and analyticity constraints, and external inputs from K-π scattering data, via the functions $H(t)$ and $G(t)$:

$$\begin{aligned} G(t) &= x \cdot G_{p1} + (1-x) \cdot G_{p2} + x \cdot (1-x) \cdot G_{p3}, \\ H(t) &= x \cdot H_{p1} + x^2 \cdot H_{p2}, \end{aligned} \tag{1.3}$$

with $x = t/(m_K - m_{\pi^0})^2$, and the numerical values of the parameters [7]:

$$\begin{aligned} &G_{p1} = 0.0209 \pm 0.0021, \quad G_{p2} = 0.0398 \pm 0.0044, \quad G_{p3} = 0.0045 \pm 0.0004, \\ &H_{p1} = (1.92^{+0.63}_{-0.32}) \cdot 10^{-3}, \quad H_{p2} = (2.63^{+0.28}_{-0.15}) \cdot 10^{-4}. \end{aligned} \tag{1.4}$$

2 Beams and detectors

Detailed descriptions of the NA48/2 beam line and detectors are available in refs. [1, 8]. Two simultaneous charged hadron beams produced by 400 GeV/c protons impinging on a beryllium target were used. Kaons represented 6% of the total beam flux and the K^+/K^- flux ratio was 1.79. Particles of opposite charge with a central momentum of 60 GeV/c and a momentum band of $\pm 3.8\%$ (RMS) were selected by a system of dipole magnets, focusing quadrupoles, muon sweepers and collimators. The decay volume was contained in a 114 m long vacuum tank with a diameter of 1.92 m for the first 66 m, and 2.40 m downstream. The two beams were superimposed in the decay volume along a common axis which defined the Z axis of the coordinate system. The Y axis pointed vertically up, and the X axis was directed horizontally to form a right-handed system.

Charged particles from $K^\pm$ decays were measured by a magnetic spectrometer consisting of four drift chambers (DCH1–DCH4) and a dipole magnet between DCH2 and

JHEP10(2018)150

	$f_+(t)$	$f_0(t)$
Taylor expansion	$1 + \lambda'_+ \frac{t}{m^2_{\pi^+}} + \frac{1}{2}\lambda''_+ \left(\frac{t}{m^2_{\pi^+}}\right)^2$	$1 + \lambda_0 \frac{t}{m^2_{\pi^+}}$
Pole	$\frac{M_V^2}{M_V^2 - t}$	$\frac{M_S^2}{M_S^2 - t}$
Dispersive	$\exp\left(\frac{\Lambda_+ + H(t)}{m^2_{\pi^+}} t\right)$	$\exp\left(\frac{\ln C - G(t)}{m_K^2 - m^2_{\pi^0}} t\right)$

Table 1. Form factor parameterizations used in this analysis. The free parameters to be measured are the λ'_+, λ''_+, λ_0 coefficients (slopes) for the Taylor expansion, the scalar M_S and vector M_V mass values for the pole model, and the Λ_+ and $\ln C$ parameters for the dispersive model.

DCH3. Each chamber consisted of four staggered double planes of sense wires measuring the coordinates transverse to the beam axis along the 0°, 90° and ±45° directions. The spectrometer was located in a tank filled with helium at nearly atmospheric pressure and separated from the vacuum tank by a 0.3% X_0 thick *Kevlar*® window. A 15.8 cm diameter evacuated aluminium tube traversing the centre of the main detectors allowed the undecayed beam particles and the muon halo from beam pion decays to continue their path in vacuum. The spectrometer momentum resolution was $\sigma_p/p = 1.02\% \oplus 0.044\% \cdot p$, with the momentum p expressed in GeV/c. The spectrometer was followed by a scintillator hodoscope (HOD) consisting of two planes segmented into horizontal and vertical strips and arranged in four quadrants.

A liquid krypton calorimeter (LKr) was used to reconstruct $\pi^0 \to \gamma\gamma$ decays and for charged particle identification. It is a 27 X_0 thick quasi-homogeneous ionization chamber with an active volume of 7 m^3 of liquid krypton, segmented transversally into 13248 2 × 2 cm^2 projective cells. It provided an energy resolution $\sigma_E/E = 0.032/\sqrt{E} \oplus 0.09/E \oplus 0.0042$, a resolution on the transverse coordinates of an isolated electromagnetic shower $\sigma_x = \sigma_y = (0.42/\sqrt{E} \oplus 0.06)$ cm, and a time resolution $\sigma_t = (2.5/\sqrt{E})$ ns, with E expressed in GeV. A hodoscope (NHOD) consisting of a plane of scintillating fibers, located inside the LKr calorimeter, was used for triggering purposes.

The LKr was followed by a hadronic calorimeter with a total iron thickness of 1.2 m. A muon detector (MUV), located further downstream, consisted of three planes of 2.7 m long and 2 cm thick scintillator strips (28 strips in total) read out by photomultipliers at both ends. Each plane was preceded by a 80 cm thick iron wall. The strips were aligned horizontally in the first and the last planes, and vertically in the second plane.

During the considered data-taking period, 4.8×10^8 events were recorded using a minimum bias trigger condition requiring a coincidence of signals in the two HOD planes in the same quadrant and an energy deposit above 10 GeV in the LKr. The data set is divided into twelve sub-samples according to the polarities of the beam line and spectrometer magnets that interchanged the paths of the positive and negative beams.

JHEP10(2018)150

3 Monte Carlo simulation

A GEANT3-based [9] Monte Carlo (MC) simulation including beam line, detector geometry and material description is used to evaluate the detector response. The beam simulation is tuned using the kaon momentum and direction distributions as measured from reconstructed $K^\pm \to \pi^\pm\pi^+\pi^-$ decays. MC samples of $K^\pm_{e3}$ ($K^\pm_{\mu3}$) decays corresponding to 3 (5) times the data samples have been produced.

The $K^\pm_{l3}$ decays are modelled according to [10] including both the Dalitz plot density of eq. (1.1) and radiative corrections, with exactly one photon emitted in each decay, and tracked through the detector if its energy in the laboratory frame is above 1 MeV. This approach takes into account the infrared divergence of photon radiation by extending the soft-photon approximation [11] to the whole energy range. The implementation has been validated in [10] using the experimental data available at the time [12, 13]: photon energy and photon-lepton angle distributions have been found to agree with the data within 1–5% systematic uncertainty. However this uncertainty includes the effect of a 100% variation of the vector FF slope. Therefore the distributions considered are not sensitive to the FF description at the level of precision required for the present study.

On the other hand, model-independent (universal) radiative corrections have been proposed in [14]. Using these corrections, the effects of model- and approximation-dependent interplay between QED and QCD are absorbed in the measured effective FFs. These FFs are free from uncertainties due to radiative corrections by construction, and their deviation from FFs defined in absence of electromagnetic interaction can be estimated within the formalism used by [14]. However this approach does not include real photon emission.

In this analysis, the approach of [10] is used, and the Dalitz plot density is corrected by event-by-event weights $w_r(E^*_l, E^*_\pi)$ equal to the ratio of densities obtained within the formulations of [14] and [10]. In the $K^\pm_{e3}$ case, the weighting leads to $d\Gamma/dE^*_e$ variations as large as 2%. In the $K^\pm_{\mu3}$ case, the weights have been found to be $w_r(E^*_\mu, E^*_\pi) = 1$ within the required precision. A linear approximation for the vector and scalar FFs $f_+(t) = f_0(t) = 1 + \ 0.0296 \cdot t/m^2_{\pi^+}$ is used to generate the simulated samples.

4 Event selection and reconstruction

Charged particles (trajectories and momenta) and LKr energy deposition clusters (energies and positions) are reconstructed as described in [1]. The energy scale correction applied to LKr clusters is established from a study of the energy-to-momentum ratio of reconstructed electrons.

4.1 Neutral pion selection

Photon candidates are defined as LKr clusters satisfying the following requirements: energy above 3 GeV; distances to impact points at the LKr front plane of each in-time (within $\pm$10 ns) track larger than 15 cm; distances to other in-time (within $\pm$5 ns) clusters larger than 10 cm. In addition, photon candidates are required to be at least 8 cm away from the LKr edges and 2 cm away from each of the 49 inactive cells to reduce the effects of energy losses.

JHEP10(2018)150

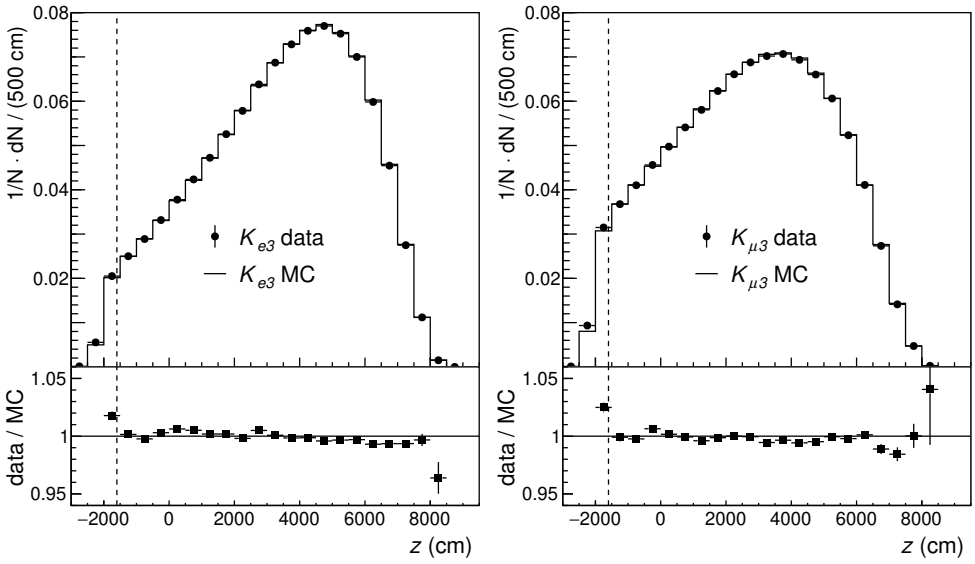

Figure 1. Distributions of the decay vertex z position for data and MC simulated samples for $K^{\pm}_{e3}$ (left) and $K^{\pm}_{\mu 3}$ (right) modes and corresponding Data/MC ratios. The simulated samples include signal and backgrounds. The vertical dashed lines indicate the cut applied (the final collimator exit is located at −1800 cm).

A pair of in-time (within ±5 ns) photon candidates is considered as a $\pi^0 \to \gamma\gamma$ decay candidate if there are no additional photon candidates within ±5 ns of their average time, the distance between them is larger than 20 cm, and the sum of their energies is at least 15 GeV. The latter condition ensures a high trigger efficiency.

The z position of the $\pi^0 \to \gamma\gamma$ decay vertex is computed from photon candidate positions and energies assuming the nominal π^0 mass [4]. It is required to be at least 2 m downstream of the final beam collimator to suppress π^0 production in the material of the collimator (figure 1). In addition, photons are required not to intercept DCH beam pipe flanges [15].

4.2 Charged lepton selection

Lepton candidates are defined as reconstructed DCH tracks satisfying the following requirements. Their momentum should be at least 5 (10) GeV/c for $e^{\pm}$ ($\mu^{\pm}$) candidates, the latter ensuring high muon identification efficiency. The distance from the track impact point at the LKr front plane to the closest inactive cell should exceed 2 cm, and the distance to the Z axis in each DCH plane should be at least 15 cm. The track should be in time (within ±10 ns) with a π^0 candidate, and no additional tracks are allowed within ±8 ns of the track.

Tracks with the ratio of LKr energy deposit E to momentum p in the range $0.9 < E/p < 2.0$ are identified as electrons ($e^{\pm}$). Tracks with $E/p < 0.9$ and associated signals in the first two MUV planes are identified as muons. Extrapolated muon track positions at the first MUV plane are required to be at least 30 (20) cm away from the Z axis (detector outer edges) to reduce geometrical inefficiencies due to multiple scattering in the preceding material.

JHEP10(2018)150

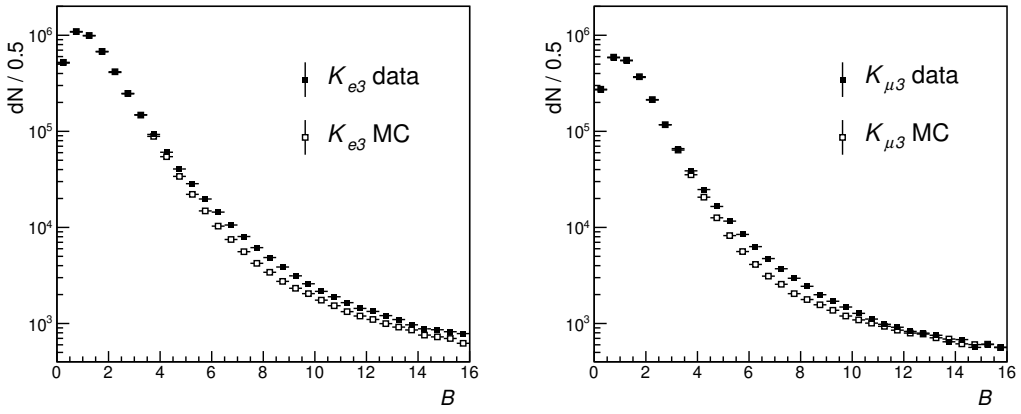

Figure 2. Distributions of the beam variable B for $K^{\pm}_{e3}$ (left) and $K^{\pm}_{\mu 3}$ (right) for data and normalized MC samples. The simulated samples include signal and backgrounds.

The $K^{\pm}_{l3}$ decay vertex is defined as follows: its z coordinate is that of the π^0 decay (section 4.1), and its transverse (x, y) coordinates are those of the lepton track at this z plane.

4.3 Beam profiles

The specific beam conditions of the data sample triggered further studies of the transverse beam profiles with fully reconstructed $K^{\pm} \to \pi^{\pm}\pi^{+}\pi^{-}$ decays. These studies showed evidence for a diverging beam component surrounding the core and giving rise to kaon decay vertices a few centimetres off the Z axis. This component, which is likely to arise from quasi-elastic kaon scattering in the beam line, is described using the following variable:

$$B = \sqrt{\left(\frac{x - x_0(z)}{\sigma_x(z)}\right)^2 + \left(\frac{y - y_0(z)}{\sigma_y(z)}\right)^2}, \tag{4.1}$$

where x, y, z are the $K^{\pm}_{l3}$ decay vertex coordinates, $x_0(z)$, $y_0(z)$ are the measured central positions of the beam profiles at the vertex z position, and $\sigma_x(z)$, $\sigma_y(z)$ are their Gaussian widths which decrease from 1 cm at the beginning to 0.6 cm at the end of the decay volume. The beam profile characteristics are obtained from reconstructed $K^{\pm} \to \pi^{\pm}\pi^{+}\pi^{-}$ decays.

The B distributions of data and MC simulated events are shown in figure 2. The data distributions are well described by simulation in the core region ($B < 3$), while the diverging beam component in the data, which is not simulated, can be seen at larger B values. Quasi-elastic scattering affects marginally the kaon momentum magnitude. Scattered beam kaons are conservatively considered in the analysis by requiring $B < 11$, which minimizes the effect of correlations between kaon directions and momenta. This condition also reduces the background from $\pi^{\pm}$ decays in flight (section 4.5).

4.4 Kaon and neutrino momenta reconstruction

A more precise estimate of the $K^{\pm}$ momentum magnitude (p_K) in the laboratory frame than the beam average value is obtained by imposing energy-momentum conservation in

JHEP10(2018)150

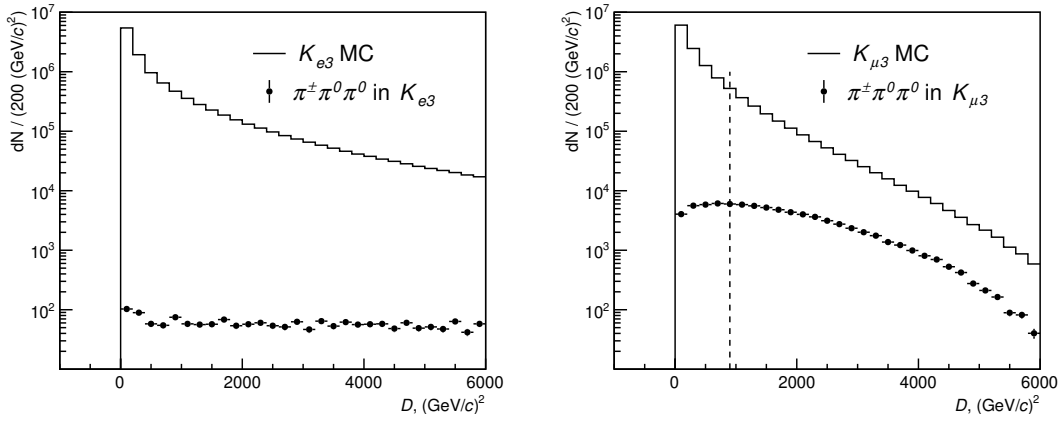

Figure 3. Distributions of the reconstructed D variable for MC simulated $K^\pm_{e3}$ (left) and $K^\pm_{\mu 3}$ (right) signal and $K^\pm \to \pi^\pm\pi^0\pi^0$ background samples. The selection condition $D < 900$ (GeV/c)^2, applied in the $K^\pm_{\mu 3}$ case for background suppression, is indicated by the vertical dashed line.

the kaon decay under the assumption of a missing neutrino, and fixing the kaon mass to its nominal value and the kaon direction to the measured beam axis direction. This leads to two solutions:

$$p_K = \frac{\psi\, p_\parallel}{E^2 - p_\parallel^2} \pm \sqrt{D}, \tag{4.2}$$

$$\text{where} \quad \psi = \frac{1}{2}\,(m_K^2 + E^2 - p_\perp^2 - p_\parallel^2), \quad D = \frac{\psi^2\, p_\parallel^2}{(E^2 - p_\parallel^2)^2} - \frac{m_K^2\, E^2 - \psi^2}{E^2 - p_\parallel^2}. \tag{4.3}$$

If D is negative due to resolution effects, a value $D = 0$ is used in the calculation. Here E, $p_\parallel$ and $p_\perp$ are the energy, longitudinal and transverse momentum components (with respect to the beam axis) of the $\pi^0 l^\pm$ system in the laboratory frame. The distributions of the D variable for MC simulated events are shown in figure 3. The solution that is closer to the average beam momentum p_B (measured from $K^\pm \to \pi^\pm\pi^+\pi^-$ decays) is chosen, and required to satisfy $|p_K - p_B| < 7.5$ GeV/c.

Distributions of the squared neutrino longitudinal momentum in the kaon rest frame, $p^2_{\nu,\parallel} = (m_K - E^*)^2 - p_\perp^2$, where E^* is the $\pi^0 l^\pm$ system energy in the kaon rest frame, are shown in figure 4. The simulated spectra are sensitive to details of the beam geometry description at small $p^2_{\nu,\parallel}$ values, and negative values originate from resolution effects. To ensure good agreement of data and simulation, it is required that $p^2_{\nu,\parallel} > 0.0014$ (GeV/c)^2 (corresponding to $p_{\nu,\parallel} > 37.4$ MeV/c) which rejects 29% of the $K^\pm_{l3}$ events in both decay modes.

4.5 Background suppression

The $K^\pm \to \pi^\pm\pi^0\pi^0$ ($\pi^0 \to \gamma\gamma$, $\pi^0 \to \gamma\gamma$) decays contribute to the background if one of the π^0 mesons is not detected, and the $\pi^\pm$ either decays or is misidentified. This background affects mainly the $K^\pm_{\mu 3}$ sample, and is reduced by requiring $D < 900$ (GeV/c)^2 in this case, as illustrated in figure 3.

JHEP10(2018)150

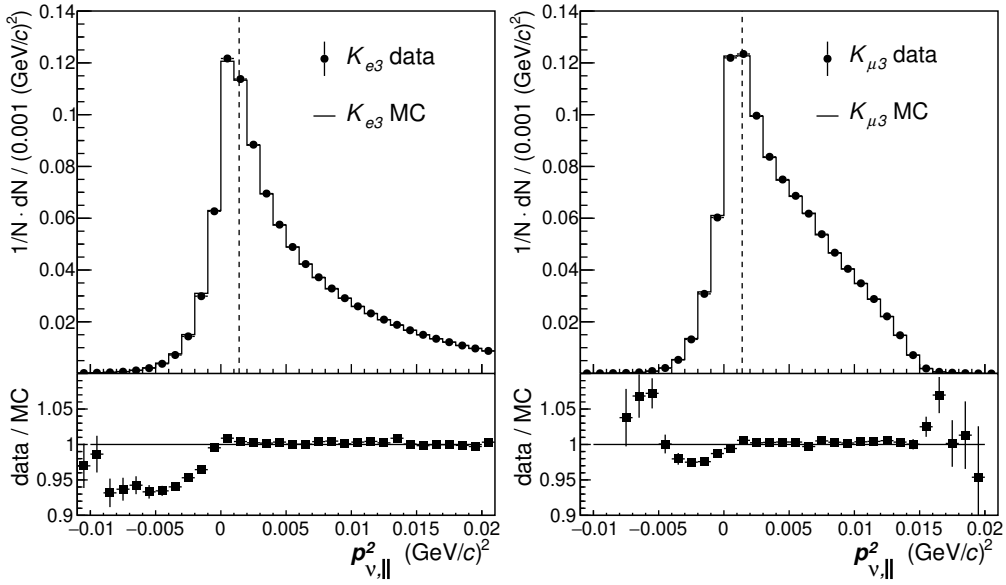

Figure 4. Normalized $p^2_{\nu,\parallel}$ distributions of data and MC simulated samples for $K^\pm_{e3}$ (left) and $K^\pm_{\mu3}$ (right) modes and corresponding Data/MC ratios. The simulated samples include signal and backgrounds. The vertical dashed lines indicate the $p^2_{\nu,\parallel} > 0.0014$ (GeV/c)^2 cut applied.

The $K^\pm \to \pi^\pm\pi^0$ background in the $K^\pm_{e3}$ sample arising from $\pi^\pm$ misidentification is characterized by small total transverse momentum and is reduced by requiring $p_{\nu,\perp} > 30$ MeV/c, taking into account resolution and beam divergence effects.

The $K^\pm \to \pi^\pm\pi^0$ background to $K^\pm_{\mu3}$ decays arises from $\pi^\pm$ misidentification and $\pi^\pm \to \mu^\pm\nu$ decay. The former process is suppressed by requiring the $\pi^0 l^\pm$ mass, reconstructed in the π^+ mass hypothesis for the lepton candidate, to be $m(\pi^\pm\pi^0) < 0.475$ GeV/c^2, which is below the K^+ mass considering the resolution of 0.003 GeV/c^2. The latter process is suppressed by requiring the reconstructed $\mu^\pm\nu$ invariant mass to be $m(\mu\nu) > 0.16$ GeV/c^2, which is above the π^+ mass considering the resolution of 0.004 GeV/c^2. Additionally, it is required that $m(\pi^\pm\pi^0)+p_{\pi^0,\perp}/c < 0.6$ GeV/c^2, where $p_{\pi^0,\perp}$ is the π^0 transverse momentum component with respect to the beam axis. The selection conditions, illustrated in figure 5, lead to 17% signal loss and reject 99.5% of the $K^\pm \to \pi^\pm\pi^0$ background.

Other background sources considered are $K^\pm \to \pi^\pm\pi^0$ followed by $\pi^0 \to e^+e^-\gamma$; $K^\pm \to \pi^\pm\pi^0\gamma$; $K^\pm \to \pi^\pm\pi^0\pi^0$ ($\pi^0 \to \gamma\gamma$, $\pi^0 \to e^+e^-\gamma$); $K^\pm \to \pi^0\pi^0 l^\pm\nu$. The $K^\pm_{\mu3}$ background to $K^\pm_{e3}$ decays arising from muon decay in flight is also considered. All these backgrounds are found to be negligible. The main background sources are summarized in table 2.

5 Form factor measurement

In total, 4.4 (2.3) $\times 10^6$ reconstructed $K^\pm_{e3}$ ($K^\pm_{\mu3}$) candidates are selected from the data sample. The Dalitz plot distributions, as defined in eq. (1.1) and based on reconstructed energies, are shown in figure 6 for the data and the main simulated backgrounds.

JHEP10(2018)150

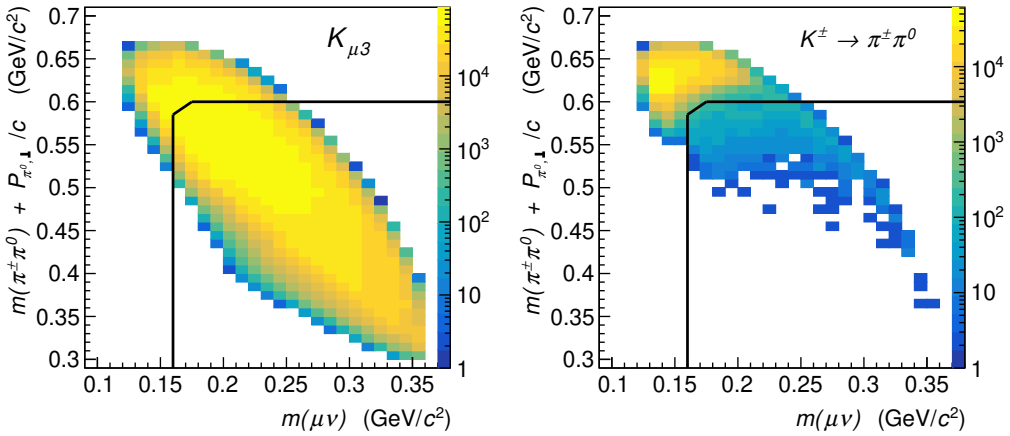

Figure 5. Distributions of the kinematic variables used for $K^{\pm} \to \pi^{\pm}\pi^0$ background suppression for MC simulated signal $K^{\pm}_{\mu 3}$ (left) and background $K^{\pm} \to \pi^{\pm}\pi^0$ (right) samples. The selection criteria are indicated by solid lines.

Process	r_e $[10^{-3}]$	r_μ $[10^{-3}]$
$K^{\pm} \to \pi^{\pm}\pi^0\pi^0$ $(\pi^0 \to \gamma\gamma, \pi^0 \to \gamma\gamma)$	0.286(6)	2.192(32)
$K^{\pm} \to \pi^{\pm}\pi^0$ $(\pi^0 \to \gamma\gamma)$	0.271(6)	0.392(10)

Table 2. Background processes and background to signal ratios r_e and r_μ in the selected $K^{\pm}_{e3}$ and $K^{\pm}_{\mu 3}$ samples, estimated from MC simulations described in section 3. The quoted errors include contributions from the external branching ratios and simulated statistics.

The FF parameters are measured independently for each of the two $K^{\pm}_{l3}$ decay modes. A joint analysis is also performed by fitting simultaneously the two Dalitz plots with a common set of FF parameters. A set of FF parameters $\vec{\lambda}$ in each parameterization is measured by minimizing an estimator

$$\chi^2(\vec{\lambda}, N) = \sum_i \frac{\left(\omega_i^{\rm data} - \omega_i^{\rm bkg}(\vec{\lambda}) - N \cdot \omega_i^{\rm sig}(\vec{\lambda})\right)^2}{\sigma^2_{\omega_i^{\rm data}} + \sigma^2_{\omega_i^{\rm bkg}}(\vec{\lambda}) + N^2 \cdot \sigma^2_{\omega_i^{\rm sig}}(\vec{\lambda})}, \tag{5.1}$$

where the sum runs over all $5 \times 5\,\mathrm{MeV}^2$ Dalitz plot cells which have their centres inside the kinematically allowed region of non-radiative $K^{\pm}_{l3}$ events and contain at least 20 reconstructed data events. Here $\omega_i^{\rm data}$ is the population in cell i of the reconstructed data Dalitz plot; $\omega_i^{\rm sig}(\vec{\lambda})$ and $\omega_i^{\rm bkg}(\vec{\lambda})$ are the expected signal and background populations estimated from simulations; $\sigma_{\omega_i^{\rm data}}$, $\sigma_{\omega_i^{\rm sig}}$ and $\sigma_{\omega_i^{\rm bkg}}$ are the corresponding statistical errors; N is a normalization factor that guarantees that the simulated sample is normalized to the data sample.

The quantities $\omega_i^{\rm sig}(\vec{\lambda})$ are obtained at each iteration by applying a weight to each simulated signal event, equal to the ratio of the Dalitz plot density corresponding to the parameter set $\vec{\lambda}$ and the generated Dalitz plot density. This approach accounts for the universal radiative corrections described in section 3. The $\vec{\lambda}$-dependence of the background contribution arises from the dependence of the signal acceptances on the FFs.

JHEP10(2018)150

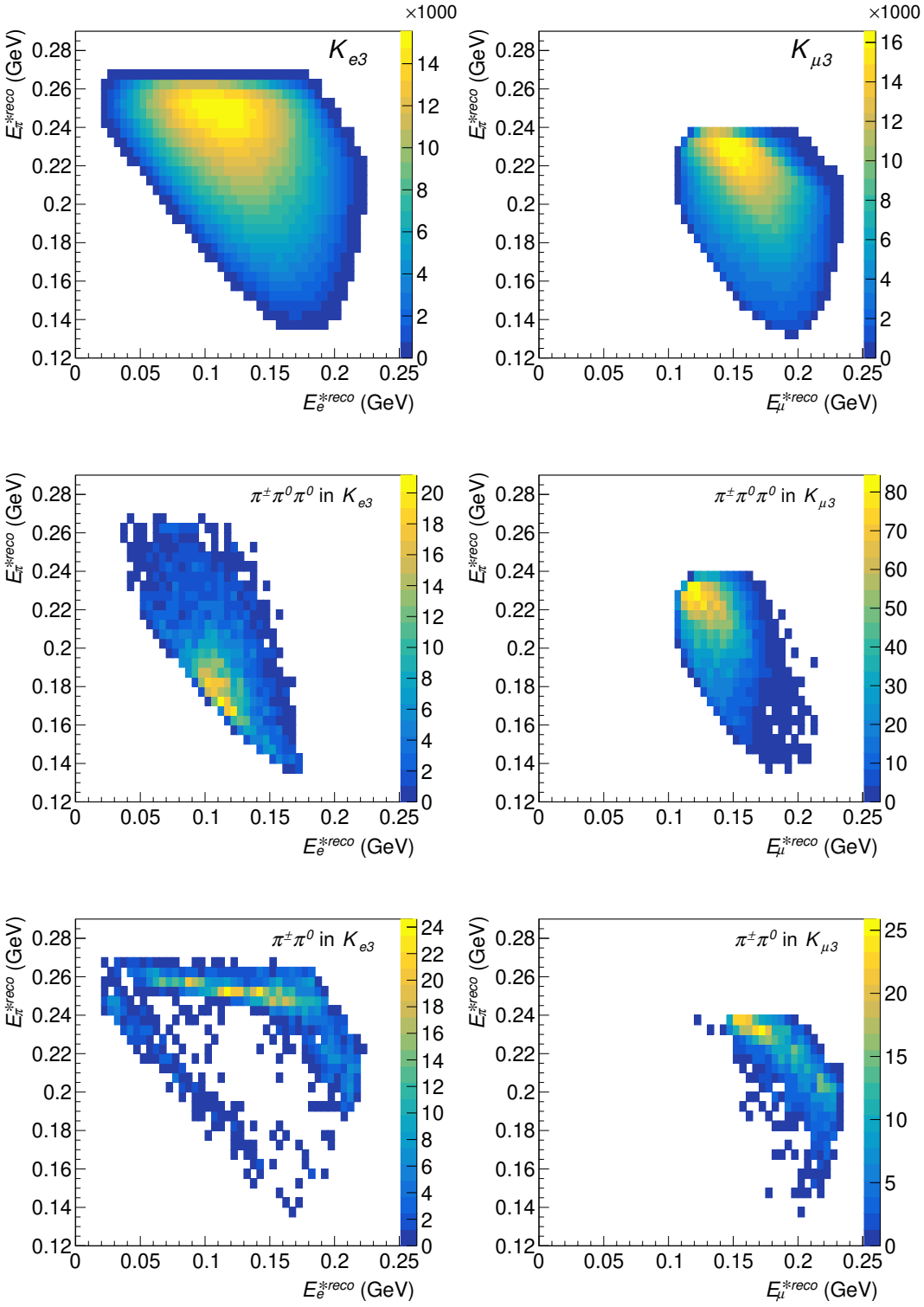

Figure 6. Dalitz plot distributions after the full selection of reconstructed $K^{\pm}_{l3}$ data events (top row), simulated $K^{\pm} \to \pi^{\pm}\pi^0\pi^0$ (middle row) and $K^{\pm} \to \pi^{\pm}\pi^0$ (bottom row) background events. Left panels correspond to the $K^{\pm}_{e3}$ selection and right panels to the $K^{\pm}_{\mu 3}$ selection. The simulated backgrounds are normalized to the total kaon flux in the data. The cell size is $5 \times 5\,\mathrm{MeV}^2$.

JHEP10(2018)150

6 Systematic uncertainties

The following sources of systematic uncertainties are considered. In each case, the analysis is repeated varying one condition at a time, and the effect on the FF parameters is quoted as a systematic uncertainty. The results are summarized in tables 3 to 5. The error estimates are conservatively assumed to be uncorrelated.

6.1 Experimental systematic uncertainties

Beam modelling. The diverging beam component which is not simulated in the NA48/2 software gives rise to one of the largest systematic effects. This effect is evaluated by adding specific samples of MC events, generated according to the measured transverse beam profile (section 4.3), to the simulated signal samples, improving the Data/MC agreement of the B spectra. The imperfect simulation of the kaon beam spectrum leads to variations of the Data/MC ratio of reconstructed momentum spectra as a function of momentum within a few percent. The corresponding systematic effect on the FF measurement is evaluated by assigning momentum-dependent weights to the simulated events and is almost negligible. To evaluate the sensitivity of the results to the beam average momentum value p_B used in the selection (section 4.4), which is reproduced by the MC simulation to a precision of 0.03 GeV/c, the analysis is repeated with the p_B value shifted conservatively by 0.1 GeV/c.

LKr energy scale and non-linearity. The π^0 reconstruction is sensitive to the LKr energy scale and non-linearities. A variation in the measured LKr energies affects the reconstructed vertex z position, and subsequently all reconstructed kinematic quantities. The systematic uncertainty on the energy scale is 0.1% (correlated between data and simulated samples) while the energy scale difference between data and simulation is known to 0.03% precision. The systematic uncertainties on the FF measurement are estimated by varying the energy scale corrections within their uncertainties. Cluster energies below 10 GeV are affected by non-linearities in the energy scale. This is corrected for, and the residual systematic effects are estimated by variation of the correction method as detailed in [15].

Residual background. Systematic uncertainties on the background estimates are evaluated by studying the level of Data/MC agreement in background-enhanced control regions defined as $0.7 < E/p < 0.9$ for the $K^{\pm}_{e3}$ selection, and $B > 15$ (corresponding to off-axis decay vertices, see section 4.3) for the $K^{\pm}_{\mu 3}$ selection. The uncertainties assigned to background contributions are $\delta r_e/r_e = 30\%$ and $\delta r_\mu/r_\mu = 10\%$. They are propagated to the results, together with those listed in table 2.

Particle identification. Electron identification efficiency is determined by the lower E/p condition. Using an almost background-free $K^{\pm}_{e3}$ data sample selected kinematically, the efficiency has been measured as a function of momentum to increase from 98% at 5 GeV/c to 99.6% above 10 GeV/c. Efficiency measurements for data and simulated samples agree to better than 0.2%. Systematic uncertainties due to electron identification are evaluated by weighting MC events to correct for the residual Data/MC disagreement. Muon identification inefficiency for $K^{\pm}_{\mu 3}$ decays is reduced to the 0.1% level, without dependence on the

JHEP10(2018)150

kinematic variables, by the minimum muon momentum and MUV geometrical acceptance requirements. The corresponding systematic effect on the FF measurement is negligible.

Event pileup. Pileup of signal events with independent kaon decays is not described by the simulation. Effects of pileup are estimated by doubling the size of the maximum allowed time difference between the accepted photon candidates, and between the accepted lepton and π^0 candidates. The shifts in the results are considered as systematic uncertainties.

Acceptance. The Data/MC ratios of the decay vertex z position distributions (figure 1) reflect the quality of the acceptance simulation. To account for the residual variation of these ratios, the transverse cuts in DCH, LKr and MUV detector planes are widened by a factor of 1.002 in the selection for the simulated samples. The resulting variations of the FF parameters are considered as systematic uncertainties.

Neutrino momentum resolution. The cut on the squared longitudinal neutrino momentum $p^2_{\nu,\parallel}$ is applied in the core region of the distribution (figure 4). A mismatch in $p^2_{\nu,\parallel}$ resolution between data and simulation can therefore bias the results. Introducing an additional smearing for the simulated events, that is increasing the deviation of the reconstructed $p^2_{\nu,\parallel}$ from its true value by 1.5%, leads to an improvement of the Data/MC agreement near the peak of the distribution. The resulting variations are taken as corresponding systematic uncertainties

Trigger efficiency. The trigger is based on uncorrelated HOD and LKr information (section 2). Within the $K^{\pm}_{l3}$ selection, the HOD trigger efficiency is measured to be 0.9973(2) using a control sample triggered by the NHOD, while the LKr trigger efficiency is measured to be 0.9987(1) using a control sample triggered by the HOD. The total trigger efficiency is obtained as the product of these two components. No statistically significant variations of the trigger efficiencies with the Dalitz plot variables are observed. Each efficiency component is measured as a function of E^*_π and E^*_l variables and parameterized with second order polynomial functions. The statistical uncertainties on the parameters of these functions are propagated to the FF measurements, and the resulting variations considered as systematic uncertainties.

Dalitz plot binning and resolution. The fit has been repeated with a Dalitz plot cell size reduced from 5×5 MeV^2 to 2.5×2.5 MeV^2. The resulting FF parameter variations stay within the statistical errors. However they are considered as systematic uncertainties to account for a possible imperfect description of the Dalitz plot density by the parameterizations. To address the resolution effects, the FF measurement has been repeated using a different method, performing a fit of the acceptance-corrected Dalitz plot by the density function (1.1). Unlike the primary fit method, this procedure introduces a bias to the results due to Dalitz plot resolution effects. This bias is estimated by performing the same fit procedure for simulated signal samples with known input FF parameters replacing the data. The differences of the fit results between the two methods, corrected for the bias, are considered as systematic uncertainties.

JHEP10(2018)150

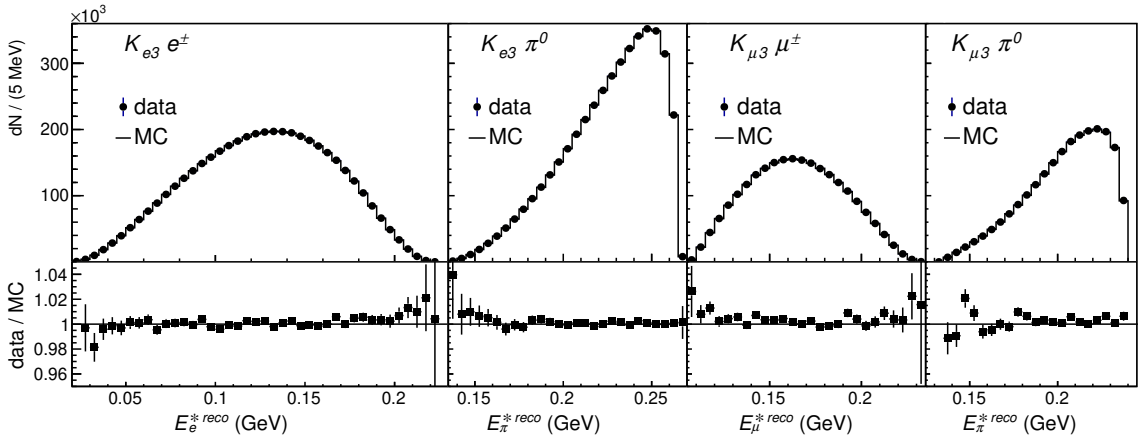

Figure 7. Reconstructed lepton energy E_l^{*reco} and pion energy E_π^{*reco} distributions for $K_{e3}^{\pm}$ and $K_{\mu 3}^{\pm}$ data (after background subtraction) and simulated samples according to the fit results using the Taylor expansion model, and corresponding Data/MC ratios. Simulated distributions according to fit results using other parameterizations cannot be distinguished within the resolution of the plots.

6.2 External sources of systematics effects

Radiative corrections. The FF parameters measured using the universal radiative corrections [14] are not affected by theoretical uncertainties by construction. Nevertheless, for comparison with other measurements and calculations, the FF fits have also been performed using radiative corrections computed within the ChPT e^2p^2 approximation [14]. The differences between the two sets of results are quoted as external uncertainties.

External inputs. The uncertainties on the numerical inputs to the dispersive parameterization (1.3) are propagated to the FF fit results under the assumption that they are not correlated.

7 Results

Lepton and pion energy projections of the reconstructed Dalitz plots for the data and the simulated samples corresponding to the fit results, along with their ratios Data/MC, are shown in figure 7. The fit results are listed in tables 3, 4 and 5 for $K_{e3}^{\pm}$, $K_{\mu 3}^{\pm}$ and the joint analysis, respectively. The fit quality is satisfactory in all cases, as quantified by the χ^2 values. The quoted correlation coefficients are derived from sums of the covariance matrices of the statistical and the systematic uncertainties. Form factor measurements performed separately for the K^+ and K^- data samples are in agreement within the statistical uncertainties. Measurements from $K_{e3}^{\pm}$ and $K_{\mu 3}^{\pm}$ decays are also in agreement.

JHEP10(2018)150

	λ'_+	λ''_+	m_V	Λ_+
Central values	24.26	1.64	885.2	24.94
Statistical error	0.78	0.30	3.3	0.21
Diverging beam component	0.89	0.31	1.4	0.10
Kaon momentum spectrum	0.00	0.00	0.1	0.01
Kaon mean momentum	0.03	0.01	0.1	0.01
LKr energy scale	0.69	0.14	5.0	0.33
LKr non-linearity	0.28	0.01	3.4	0.22
Residual background	0.08	0.04	0.4	0.02
Electron identification	0.02	0.01	0.2	0.01
Event pileup	0.24	0.08	0.5	0.03
Acceptance	0.29	0.08	1.2	0.08
Neutrino momentum resolution	0.18	0.04	1.1	0.07
Trigger efficiency	0.33	0.13	1.0	0.07
Dalitz plot binning	0.07	0.01	0.7	0.05
Dalitz plot resolution	0.06	0.04	0.4	0.02
Radiative corrections	0.20	0.01	2.9	0.19
External inputs				0.44
Systematic error	1.30	0.39	7.2	0.64
Total error	1.51	0.49	7.9	0.67
Correlation coefficient	-0.929		—	—
χ^2/NDF	569.1/687		568.9/688	569.0/688

Table 3. Form factor results of the $K^{\pm}_{e3}$ analysis. The correlation includes both statistical and systematic uncertainties. The units of λ'_+, λ''_+ and Λ_+ values and errors are 10^{-3}. The units of m_V value and error are MeV/c^2.

JHEP10(2018)150

	λ'_+	λ''_+	λ_0	m_V	m_S	Λ_+	$\ln C$
Central values	24.27	1.83	14.20	878.4	1214.8	25.36	182.17
Statistical error	2.88	1.05	1.14	8.8	23.5	0.58	6.31
Diverging beam component	2.03	0.78	0.13	0.9	30.9	0.04	8.98
Kaon momentum spectrum	0.08	0.02	0.00	0.1	0.9	0.01	0.24
Kaon mean momentum	0.06	0.00	0.06	0.8	2.4	0.06	0.63
LKr energy scale	0.31	0.01	0.53	4.5	19.4	0.30	5.55
LKr non-linearity	0.93	0.38	0.25	1.3	21.7	0.08	6.26
Residual background	0.13	0.00	0.02	1.7	1.3	0.11	0.31
Event pileup	0.04	0.01	0.03	0.0	0.7	0.00	0.18
Acceptance	0.70	0.18	0.18	2.9	0.3	0.20	0.14
Neutrino momentum resolution	0.09	0.03	0.08	0.2	2.1	0.01	0.59
Trigger efficiency	0.60	0.08	0.23	5.1	5.7	0.35	1.72
Dalitz plot binning	1.50	0.63	0.63	2.8	3.6	0.18	0.85
Dalitz plot resolution	0.04	0.01	0.02	0.1	0.4	0.01	0.18
Radiative corrections	0.32	0.10	0.54	0.7	23.7	0.04	6.73
External inputs						0.46	2.87
Systematic error	2.89	1.09	1.07	8.3	49.2	0.72	14.45
Total error	4.08	1.52	1.57	12.1	54.5	0.92	15.76
Correlation coefficients	-0.974 (λ'_+/λ''_+)			0.029		0.104	
	0.511 (λ'_+/λ_0)						
	-0.513 (λ''_+/λ_0)						
χ^2/NDF	409.9/381			409.9/382		410.3/382	

Table 4. Form factor results of the $K^{\pm}_{\mu 3}$ analysis. The correlations include both statistical and systematic uncertainties. The units of λ'_+, λ''_+, λ_0, Λ_+ and $\ln C$ values and errors are 10^{-3}. The units of m_V and m_S values and errors are MeV/c^2.

JHEP10(2018)150

	λ'_+	λ''_+	λ_0	m_V	m_S	Λ_+	$\ln C$
Central values	24.24	1.67	14.47	884.4	1208.3	24.99	183.65
Statistical error	0.75	0.29	0.63	3.1	21.2	0.20	5.92
Diverging beam component	0.97	0.35	0.55	1.1	32.2	0.08	9.43
Kaon momentum spectrum	0.00	0.00	0.02	0.1	0.7	0.00	0.19
Kaon mean momentum	0.04	0.01	0.04	0.2	1.7	0.01	0.47
LKr energy scale	0.66	0.12	0.61	4.9	17.4	0.32	5.16
LKr non-linearity	0.20	0.01	0.55	3.1	19.6	0.20	5.77
Residual background	0.08	0.03	0.04	0.1	0.7	0.01	0.16
Electron identification	0.01	0.01	0.01	0.2	0.2	0.01	0.05
Event pileup	0.23	0.08	0.08	0.4	0.2	0.03	0.07
Acceptance	0.23	0.07	0.03	0.7	4.3	0.05	1.11
Neutrino momentum resolution	0.16	0.04	0.04	0.9	3.3	0.06	0.88
Trigger efficiency	0.29	0.13	0.20	1.1	9.9	0.07	2.82
Dalitz plot binning	0.05	0.04	0.06	0.9	1.1	0.06	0.29
Dalitz plot resolution	0.02	0.01	0.03	0.0	1.3	0.00	0.39
Radiative corrections	0.17	0.01	0.57	2.5	20.1	0.16	5.92
External inputs						0.44	2.94
Systematic error	1.30	0.41	1.17	6.7	47.5	0.62	14.25
Total error	1.50	0.50	1.32	7.4	52.1	0.65	15.43
Correlation coefficient	-0.934 (λ'_+/λ''_+)			0.374		0.354	
	0.118 (λ'_+/λ_0)						
	0.091 (λ''_+/λ_0)						
χ^2/NDF	979.6/1070			979.3/1071		979.7/1071	

Table 5. Form factor results of the joint $K^{\pm}_{l3}$ analysis. The correlations include both statistical and systematic uncertainties. The units of λ'_+, λ''_+, λ_0, Λ_+ and $\ln C$ values and errors are 10^{-3}. The units of m_V and m_S values and errors are MeV/c^2.

JHEP10(2018)150

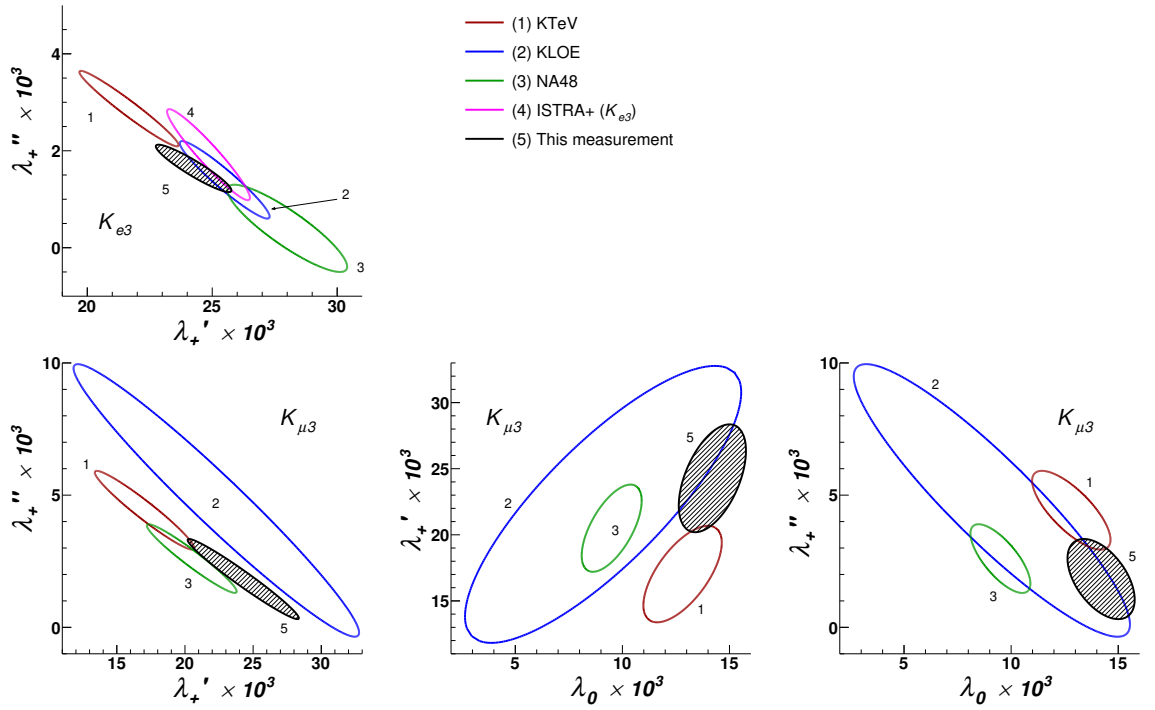

Figure 8. One sigma (39.4% CL) contours for the obtained parameters of the Taylor expansion of the K_{e3} and $K_{\mu 3}$ FFs together with measurements (obtained from K_L^0 or K^- decays) by the KTeV [16], KLOE [17, 18], NA48 [19, 20], and ISTRA+ [21, 22] Collaborations. The K_{e3} results from NA48 and ISTRA+ have been modified by [2] to comply with the considered parameterization. The $K_{\mu 3}$ results from ISTRA+ do not provide enough information to be displayed on the same panels as the other experimental results.

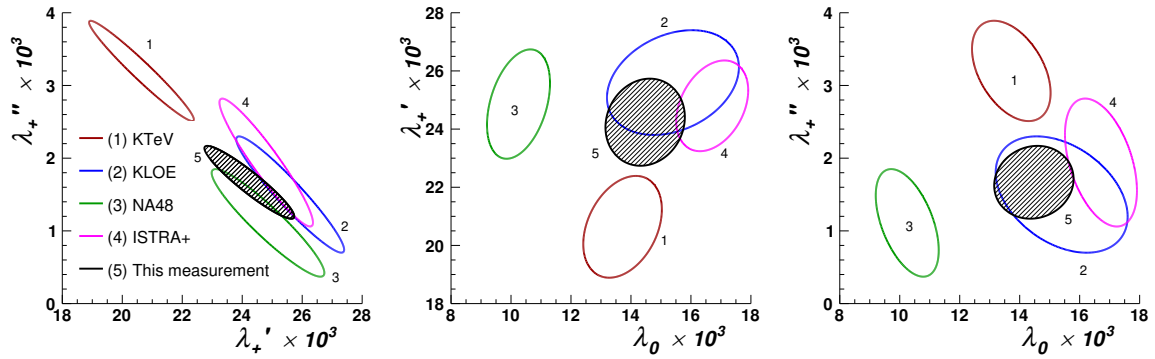

Figure 9. One sigma (39.4% CL) contours for the parameters of the Taylor expansion obtained from the joint analysis together with the combinations of K_{e3} and $K_{\mu 3}$ measurements by the KTeV [16], KLOE [17, 18], NA48 [19, 20], and ISTRA+ [21, 22] Collaborations provided by [2].

The results of the present analysis for the Taylor expansion parameterization, together with the earlier results from KTeV [16], KLOE [17, 18], NA48 [19, 20], and ISTRA+ [21, 22] experiments, as reviewed in [2], are shown in figures 8, 9. The present results are in agreement with the previous measurements and have similar or better precision.

JHEP10(2018)150

Acknowledgments

We gratefully acknowledge the CERN SPS accelerator and beam line staff for the excellent performance of the beam and the technical staff of the participating institutes for their efforts in the maintenance and operation of the detector, and data processing. We are grateful to Matthew Moulson for useful discussions.

JHEP10(2018)150

References

[1] NA48/2 collaboration, J.R. Batley et al., *Search for direct CP-violating charge asymmetries in $K^{\pm} \to \pi^{\pm}\pi^{+}\pi^{-}$ and $K^{\pm} \to \pi^{\pm}\pi^{0}\pi^{0}$ decays*, *Eur. Phys. J.* **C 52** (2007) 875 [arXiv:0707.0697] [INSPIRE].

[2] FlaviaNet Working Group on Kaon Decays collaboration, M. Antonelli et al., *An evaluation of $|V_{us}|$ and precise tests of the Standard Model from world data on leptonic and semileptonic kaon decays*, *Eur. Phys. J.* **C 69** (2010) 399 [arXiv:1005.2323] [INSPIRE].

[3] L.M. Chounet, J.-M. Gaillard and M.-K. Gaillard, *Leptonic decays of hadrons*, *Phys. Rept.* **4** (1972) 199 [INSPIRE].

[4] Particle Data Group collaboration, M. Tanabashi et al., *Review of particle physics*, *Phys. Rev.* **D 98** (2018) 030001 [INSPIRE].

[5] P. Dennery and H. Primakoff, *Three-body leptonic decays of the K mesons*, *Phys. Rev.* **131** (1963) 1334.

[6] P. Lichard, *Some implications of meson dominance in weak interactions*, *Phys. Rev.* **D 55** (1997) 5385 [hep-ph/9702345] [INSPIRE].

[7] V. Bernard, M. Oertel, E. Passemar and J. Stern, *Dispersive representation and shape of the K_{l3} form factors: robustness*, *Phys. Rev.* **D 80** (2009) 034034 [arXiv:0903.1654] [INSPIRE].

[8] NA48 collaboration, V. Fanti et al., *The beam and detector for the NA48 neutral kaon CP-violations experiment at CERN*, *Nucl. Instrum. Meth.* **A 574** (2007) 433 [INSPIRE].

[9] R. Brun et al., *GEANT detector description and simulation tool*, CERN program library long writeup CERN-W5013, CERN, Geneva, Switzerland, (1994) [INSPIRE].

[10] C. Gatti, *Monte Carlo simulation for radiative kaon decays*, *Eur. Phys. J.* **C 45** (2006) 417 [hep-ph/0507280] [INSPIRE].

[11] S. Weinberg, *Infrared photons and gravitons*, *Phys. Rev.* **140** (1965) B516 [INSPIRE].

[12] KTeV collaboration, T. Alexopoulos et al., *Measurements of the branching fractions and decay distributions for $K_L \to \pi^{\pm}\mu^{\mp}\nu\gamma$ and $K_L \to \pi^{\pm}e^{\mp}\nu\gamma$*, *Phys. Rev.* **D 71** (2005) 012001 [hep-ex/0410070] [INSPIRE].

[13] NA48 collaboration, A. Lai et al., *Measurement of the radiative K_{e3} branching ratio*, *Phys. Lett.* **B 605** (2005) 247 [hep-ex/0411069] [INSPIRE].

[14] V. Cirigliano, M. Knecht, H. Neufeld, H. Rupertsberger and P. Talavera, *Radiative corrections to K_{l3} decays*, *Eur. Phys. J.* **C 23** (2002) 121 [hep-ph/0110153] [INSPIRE].

[15] J.R. Batley et al., *Determination of the S-wave $\pi\pi$ scattering lengths from a study of $K^{\pm} \to \pi^{\pm}\pi^0\pi^0$ decays*, *Eur. Phys. J.* **C 64** (2009) 589 [arXiv:0912.2165] [INSPIRE].

[16] KTeV collaboration, T. Alexopoulos et al., *Measurements of semileptonic K_L decay form-factors*, *Phys. Rev.* **D 70** (2004) 092007 [hep-ex/0406003] [INSPIRE].

[17] KLOE collaboration, F. Ambrosino et al., *Measurement of the form-factor slopes for the decay $K_L \to \pi^{\pm}e^{\mp}\nu$ with the KLOE detector*, *Phys. Lett.* **B 636** (2006) 166 [hep-ex/0601038] [INSPIRE].

[18] KLOE collaboration, F. Ambrosino et al., *Measurement of the $K_L \to \pi\mu\nu$ form-factor parameters with the KLOE detector*, *JHEP* **12** (2007) 105 [arXiv:0710.4470] [INSPIRE].

[19] NA48 collaboration, A. Lai et al., *Measurement of K^0_{e3} form-factors*, *Phys. Lett.* **B 604** (2004) 1 [hep-ex/0410065] [INSPIRE].

[20] NA48 collaboration, A. Lai et al., *Measurement of $K^0_{\mu 3}$ form factors*, *Phys. Lett.* **B 647** (2007) 341 [hep-ex/0703002] [INSPIRE].

[21] ISTRA+ collaboration, O.P. Yushchenko et al., *High statistic study of the $K^- \to \pi^0\mu^-\nu$ decay*, *Phys. Lett.* **B 581** (2004) 31 [hep-ex/0312004] [INSPIRE].

[22] ISTRA+ collaboration, O.P. Yushchenko et al., *High statistic measurement of the $K^- \to \pi^0 e^-\nu$ decay form-factors*, *Phys. Lett.* **B 589** (2004) 111 [hep-ex/0404030] [INSPIRE].

JHEP10(2018)150

The NA48/2 collaboration

Cavendish Laboratory, University of Cambridge, Cambridge, CB3 0HE, U.K. [3]
J.R. Batley, G. Kalmus, C. Lazzeroni [1,2], D.J. Munday [1], M.W. Slater [1], S.A. Wotton

CERN, CH-1211 Genève 23, Switzerland
R. Arcidiacono [4], G. Bocquet, N. Cabibbo †, A. Ceccucci, D. Cundy [5],
V. Falaleev [6], M. Fidecaro, L. Gatignon, A. Gonidec, W. Kubischta,
A. Maier, A. Norton [7], M. Patel [8], A. Peters

Joint Institute for Nuclear Research, 141980 Dubna (MO), Russia
S. Balev †, P.L. Frabetti, E. Gersabeck [9], E. Goudzovski [1,2,10], P. Hristov [11],
V. Kekelidze, V. Kozhuharov [12,13], L. Litov [12], D. Madigozhin *, N. Molokanova,
I. Polenkevich, Yu. Potrebenikov, S. Shkarovskiy *, S. Stoynev [14], A. Zinchenko †

The Enrico Fermi Institute, The University of Chicago, Chicago, IL 60126, U.S.A.
E. Monnier [15], E. Swallow †, R. Winston [16]

Department of Physics and Astronomy, University of Edinburgh, Edinburgh, EH9 3JZ, U.K.
P. Rubin [17], A. Walker

Dipartimento di Fisica e Scienze della Terra dell'Università e Sezione dell'INFN di Ferrara, I-44122 Ferrara, Italy
P. Dalpiaz, C. Damiani, M. Fiorini, M. Martini, F. Petrucci, M. Savrié, M. Scarpa, H. Wahl

Sezione dell'INFN di Ferrara, I-44122 Ferrara, Italy
W. Baldini, A. Cotta Ramusino, A. Gianoli

Dipartimento di Fisica dell'Università e Sezione dell'INFN di Firenze, I-50125 Sesto Fiorentino, Italy
M. Calvetti, E. Celeghini, E. Iacopini, M. Lenti, G. Ruggiero [18]

Sezione dell'INFN di Firenze, I-50019 Sesto Fiorentino, Italy
A. Bizzeti [19], M. Veltri [20]

Institut für Physik, Universität Mainz, D-55099 Mainz, Germany [21]
M. Behler, K. Eppard, M. Hita-Hochgesand, K. Kleinknecht, P. Marouelli, L. Masetti,
U. Moosbrugger, C. Morales Morales, B. Renk, M. Wache, R. Wanke, A. Winhart [1]

Department of Physics and Astronomy, Northwestern University, Evanston, IL 60208, U.S.A.
D. Coward [22], A. Dabrowski [11], T. Fonseca Martin, M. Shieh, M. Szleper [23], M. Velasco,
M.D. Wood [22]

Dipartimento di Fisica dell'Università e Sezione dell'INFN di Perugia, I-06100 Perugia, Italy
G. Anzivino, E. Imbergamo, A. Nappi †, M. Piccini, M. Raggi [24], M. Valdata-Nappi

JHEP10(2018)150

Sezione dell'INFN di Perugia, I-06100 Perugia, Italy
P. Cenci, M. Pepe, M.C. Petrucci

Dipartimento di Fisica dell'Università e Sezione dell'INFN di Pisa, I-56100 Pisa, Italy
F. Costantini, N. Doble, L. Fiorini [25], S. Giudici, G. Pierazzini †, M. Sozzi, S. Venditti

Scuola Normale Superiore e Sezione dell'INFN di Pisa, I-56100 Pisa, Italy
G. Collazuol [26], L. DiLella [27], G. Lamanna [27], I. Mannelli, A. Michetti

Sezione dell'INFN di Pisa, I-56100 Pisa, Italy
C. Cerri, R. Fantechi

DSM/IRFU — CEA Saclay, F-91191 Gif-sur-Yvette, France
B. Bloch-Devaux [28], C. Cheshkov [29], J.B. Chèze, M. De Beer, J. Derré, G. Marel, E. Mazzucato, B. Peyaud, B. Vallage

Fachbereich Physik, Universität Siegen, D-57068 Siegen, Germany [30]
M. Holder, M. Ziolkowski

Dipartimento di Fisica dell'Università e Sezione dell'INFN di Torino, I-10125 Torino, Italy
S. Bifani [1], M. Clemencic [11], S. Goy Lopez [31]

Sezione dell'INFN di Torino, I-10125 Torino, Italy
C. Biino, N. Cartiglia, F. Marchetto

Österreichische Akademie der Wissenschaften, Institut für Hochenergiephysik, A-10560 Wien, Austria [32]
H. Dibon, M. Jeitler, M. Markytan, I. Mikulec, G. Neuhofer, L. Widhalm †

*: Corresponding authors
†: Deceased

1: Now at: School of Physics and Astronomy, University of Birmingham, Birmingham, B15 2TT, U.K.
2: Supported by a Royal Society University Research Fellowship (UF100308, UF0758946)
3: Funded by the U.K. Particle Physics and Astronomy Research Council, grant PPA/G/O/1999/00559
4: Now at: Università degli Studi del Piemonte Orientale e Sezione dell'INFN di Torino, I-10125 Torino, Italy
5: Now at: Istituto di Cosmogeofisica del CNR di Torino, I-10133 Torino, Italy
6: Now at: Joint Institute for Nuclear Research, 141980 Dubna (MO), Russia
7: Now at: Dipartimento di Fisica e Scienze della Terra dell'Università e Sezione dell'INFN di Ferrara, I-44122 Ferrara, Italy
8: Now at: Department of Physics, Imperial College, London, SW7 2BW, U.K.
9: Now at: School of Physics and Astronomy, The University of Manchester, Manchester, M13 9PL, U.K.
10: Supported by ERC Starting Grant 336581

JHEP10(2018)150

11: Now at: CERN, CH-1211 Genève 23, Switzerland
12: Now at: Faculty of Physics, University of Sofia "St. Kl. Ohridski", BG-1164 Sofia, Bulgaria, funded by the Bulgarian National Science Fund under contract DID02-22
13: Also at: Laboratori Nazionali di Frascati, I-00044 Frascati, Italy
14: Now at: Fermi National Accelerator Laboratory, Batavia, IL 60510, U.S.A.
15: Now at: Centre de Physique des Particules de Marseille, IN2P3-CNRS, Université de la Méditerranée, F-13288 Marseille, France
16: Now at: School of Natural Sciences, University of California, Merced, CA 95343, U.S.A.
17: Now at: School of Physics, Astronomy and Computational Sciences, George Mason University, Fairfax, VA 22030, U.S.A.
18: Now at: Physics Department, University of Lancaster, Lancaster, LA1 4YW, U.K.
19: Also at Dipartimento di Scienze Fisiche, Informatiche e Matematiche, Università di Modena e Reggio Emilia, I-41125 Modena, Italy
20: Also at Istituto di Fisica, Università di Urbino, I-61029 Urbino, Italy
21: Funded by the German Federal Minister for Education and research under contract 05HK1UM1/1
22: Now at: SLAC, Stanford University, Menlo Park, CA 94025, U.S.A.
23: Now at: National Center for Nuclear Research, P-05-400 Świerk, Poland
24: Now at: Università di Roma "La Sapienza", I-00185 Roma, Italy
25: Now at: Instituto de Física Corpuscular IFIC, Universitat de València, E-46071 València, Spain
26: Now at: Dipartimento di Fisica dell'Università e Sezione dell'INFN di Padova, I-35131 Padova, Italy
27: Now at: Dipartimento di Fisica dell'Università e Sezione dell'INFN di Pisa, I-56100 Pisa, Italy
28: Now at: Dipartimento di Fisica dell'Università di Torino, I-10125 Torino, Italy
29: Now at: Institut de Physique Nucléaire de Lyon, IN2P3-CNRS, Université Lyon I, F-69622 Villeurbanne, France
30: Funded by the German Federal Minister for Research and Technology (BMBF) under contract 056SI74
31: Now at: Centro de Investigaciones Energeticas Medioambientales y Tecnologicas, E-28040 Madrid, Spain
32: Funded by the Austrian Ministry for Traffic and Research under the contract GZ 616.360/2-IV GZ 616.363/2-VIII, and by the Fonds für Wissenschaft und Forschung FWF Nr. P08929-PHY

JHEP10(2018)150